Acta Materialia 265 (2024) 119606

Contents lists available at ScienceDirect

Acta Materialia

journal homepage: www.elsevier.com/locate/actamat

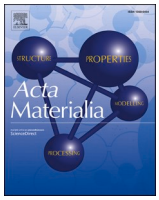

Full length article

Core shift controls grain boundary energy scaling in Cu and Al

Xiaopu Zhang *, John J. Boland *

Centre for Research on Adaptive Nanostructures and Nanodevices (CRANN), AMBER SFI Research Centre and School of Chemistry, Trinity College Dublin, Dublin 2, Ireland

ARTICLE INFO

Keywords:
Grain boundary energy
Molecular statics simulations
Grain boundary core

ABSTRACT

Grain boundary energies in different elements are correlated. The proportional scaling constants relating the energies of crystallography-equivalent boundaries in any two f.c.c. elements are nearly constant, with the notable exception of aluminum where these constants are known to vary significantly. However, the origins of the exceptional behavior of aluminum are not understood. Previously, we reported that for fcc metals there is a preference for tilt boundaries to shift their tilt axis across the $(1\bar{1}0)$ plane towards [112] and to ultimately form low energy [112] core shifted boundaries (CSBs). By comparing grain boundary energies in copper and aluminum with different tilt axes in $(1\bar{1}0)$ plane, we now report the existence of a well-defined scaling behavior for the case of low angle boundaries. In contrast, the scaling constant for high angle boundaries is essentially fixed regardless of their tilt axis shift. This results in a gradual change in the scaling constants from low angle to high angle boundaries, which is responsible for the apparent exceptional scaling behavior found in aluminum. An analysis of structure evolution during core shifting points to the significance of boundary-core dissociation, a form of correlated relaxation of individual atoms at boundaries, in controlling the scaling of boundary energies.

1. Introduction

A fundamental goal of materials science is to understand the structure-property relationship, such as that between the macroscopic and microscopic structures of grain boundaries and their energies. The dependence of boundary energies on boundary geometrical parameters plays an important role in driving microstructure evolution in the bulk and close to surfaces [1–9]. Organizing data by examining scaling trends and correlation is interesting and useful, and important new insights can be gained by discovering the underlying physics for these correlations, which in turn can predict behaviors in related systems. For example, the universal equation of state for metals was discussed a long time ago, and the scaled binding energy for all metals can be brought onto the same curve as a function of scaled atom separation [10,11]. Later, EAM potential based calculation revealed the scaling of elemental-metal grain-boundary energies with the shear modulus of metals [3]. Recently, much attention has been focused on energies for crystallography-equivalent (CE) boundaries, which have the same geometric thermodynamic variables – 5 macroscopic degrees of freedom. The 5 degrees of freedom includes lattice rotation and bicrystal section. The former is defined by axis and (misorientation) angle. The latter is described by the sectioning plane. Atomic simulation reveals that the energies of CE boundaries in different elemental metals show near perfect proportional scaling [3–9], suggesting a functional relationship between boundary energies and the 5 geometric variables. The actual functional form was ultimately developed in year 2014 [7].

Among the many proportional relationships between pairs of fcc metals, the scaling of boundary energies involving Al always show significant scatter from the proportional line and hence the behavior cannot be described by a well-defined scaling constant. Understanding the origins of this behavior is extremely challenging since 5 geometric thermodynamic variables and many material parameters are possibly involved [12] and hence it is difficult to distinguish different kinds of contribution. While it is established that Al is different from other fcc metals, with a low elastic anisotropy such as $2C_{44}/(C_{11}-C_{12})$ and a high stacking fault energy Γ, the role these differences play in the observed scaling behavior has never been addressed. On the other hand, it is well known that grains can rotate in nanocrystalline materials, such as metal thin films and nanowires which are both of technological importance [13]. The change of the rotation axis or angle during grain rotation gives rise to boundary core shifting [14] and misorientation angle variations. Furthermore, recent progress on grain boundary kinetics also revealed the widespread existence of grain rotation in bulk polycrystal materials [15,16]. However, the effect of boundary core shifting on the physical

* Corresponding authors.
E-mail addresses: xiaopuz@tcd.ie (X. Zhang), jboland@tcd.ie (J.J. Boland).

https://doi.org/10.1016/j.actamat.2023.119606
Received 18 October 2023; Received in revised form 23 November 2023; Accepted 12 December 2023
Available online 14 December 2023

properties, such as boundary energies and their scaling behaviors, has to this point been completely ignored.

Nonetheless the puzzling behavior of aluminum with other fcc metals is readily observed in the boundary-energy calculations with empirical potentials, which are capable of capturing important physical properties in metals, such as stacking fault energies and widths [3,5]. Advanced calculations, which more accurately reproduce these same physical properties, are expected to highlight the same behavior [17–20].

Here we studied the energy of Al boundaries with tilt axes from [110], through [111] and [112] to [001] in $(1\bar{1}0)$ plane, taking the corresponding Cu boundary energies as reference. We found that the scaling constant for low angle boundaries depends on the extent to which the tilt axes of these boundaries are shifted from the [112] direction in the close packed plane, which we previously showed is always the lowest energy boundary for fcc metals regardless of the in-plane misorientation angle [14,21–24]. Tilt axes that are aligned along the [112] direction have cores that lie within single close packed $(11\bar{1})$ planes, facilitating in the cases of low angle Cu and Al boundaries the maximum level of dissociation and relaxation, respectively, which yields the smallest possible scaling constant.

2. Method

Boundary structures and their energies are determined by boundary geometries, microscopic shifts and individual atomic relaxations [1]. The effect of microscopic shifts was eliminated through structural searches that explored hundreds of different possible shifts and only the lowest energy boundaries are considered [1,2]. We performed the structural searches through rigid body translation for the initial structures followed by structure optimization [8,25,26]. Hence, this allowed us to focus on the effect of individual atomic relaxations, and the influence of boundary microstructures on boundary energies.

We begin by considering symmetric [111] tilt boundaries, shown in Fig. 1(b), with in-plane misorientation angle θ and $(1\bar{1}0)$ mean boundary plane [14,21–24]. The black and white crystal lattices are obtained from the median lattice (see Fig. 1a) by equal and opposite rotation $\pm\theta/2$, respectively, as illustrated in Fig. 1(b). We calculated the boundary energies in the bulk for copper, aluminum, nickel, gold, and platinum at different core shift angles ψ, which is the angular shift (inclination) of the boundary core or the composite rotation axis l away from [111] as the composite rotation axis shifts across the $(1\bar{1}0)$ boundary plane [21]. We exploit here our boundary analysis shown in Fig. 1(c) [21], which, in contrast to previous one [14], is based on the boundary-core orientation or tilt axis direction and greatly facilities the computation. The composite rotation axis l and the core-shift angle ψ are shown in Fig. 1(c), which also shows the composite period vector p.

The composite rotation results from two consecutive rotations [1,14,21,27]. As shown in Fig. 1(a) and (b), the first rotation is defined by [111] tilt axis, an in-plane misorientation angle θ, and mean boundary plane $(1\bar{1}0)$. Fig. 1(c) show the second rotation involves an out-of-plane rotation along the period vector of the previous boundary (x axis direction in the figure), and gives rise to a tilt boundary with composite rotation axes l in the $(1\bar{1}0)$ plane, a composite misorientation angle γ and also a mean boundary plane $(1\bar{1}0)$ [1,14,21,27]. In summary, the composite rotation axis l is the rotation axis after two consecutive rotations of the two lattices [14]. The second rotation shifts the axis away from [111]. Thus, there is a core shift angle ψ between the [111] and the composite rotation axis after out-of-plane rotation [21].

To clearly illustrate the boundary geometry discussed above, we show in Fig. 1(d) the cross-section view of one copper boundary plane (xz plane with its boundary normal along the y direction) with atoms on the $+y$ side removed. The grain boundary cores are selected by the

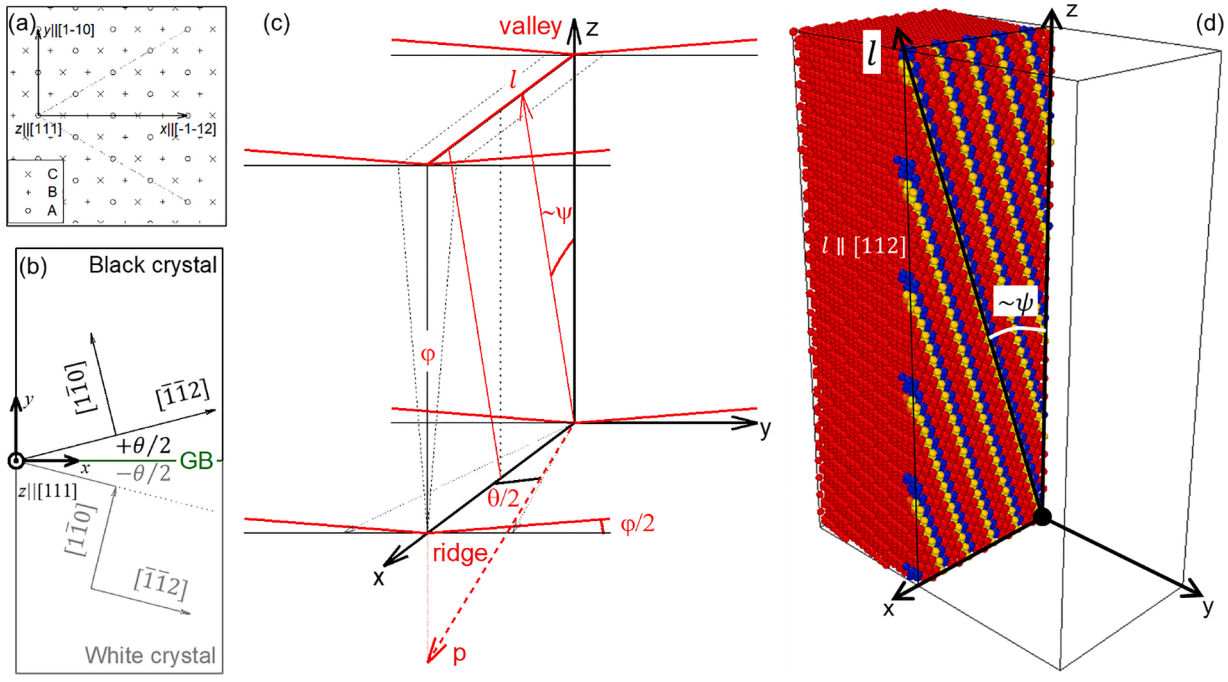

Fig. 1. Boundary geometry

(a) median lattice adhering to the xyz coordination system. (b) black and white bicrystals and their own coordination systems are rotated $\pm\boldsymbol{\theta}/2$ along axis z or [111] direction of the median lattice, respectively. (c) out-of-plane rotation $\boldsymbol{\varphi}$, shifting the axis $\boldsymbol{l}$ of the composite rotation $(\boldsymbol{l},\boldsymbol{\gamma})$ from [111] direction, where $\boldsymbol{\gamma}$ is the composite rotation angle (not shown in the figure). The composite period vector is $\boldsymbol{p}$ and the composite boundary normal is still along y. (d) cross-section view of one copper boundary plane (xz plane with its boundary normal along y direction) with atoms on the $+y$ side removed. The grain boundary cores are selected by the centrosymmetry parameter and colored differently from red atoms at fcc sites, and lie along the composite rotation axis $\boldsymbol{l}$. This boundary is obtained from GB13.17 with rotation axis [111] and in-plane misorientation angle $\boldsymbol{\theta} = 13.17^{\circ}$, followed by an out-of-plane rotation $\tan(\boldsymbol{\varphi}/2) = 1/(4\sqrt{38})$. Its composite rotation axis $\boldsymbol{l}$ is [112] and its composite rotation angle $\boldsymbol{\gamma}$ is 13.96°. The core-shift angle $\boldsymbol{\psi}$ is 19.47°.

centrosymmetry parameter and colored differently from red atoms at fcc sites, and lie along the composite rotation axis *l*. This boundary is obtained from GB13.17 with rotation axis [111] and in-plane misorientation angle $\theta = 13.17°$, followed by an out-of-plane rotation $\tan(\varphi/2) = 1/(4\sqrt{38})$. Its composite rotation axis *l* is [112] and its composite rotation angle γ is 13.96° The core-shift angle ψ is 19.47°

We performed these calculations for 20 different in-plane misorientation angles θ [21] and for each in-plane misorientation angle 20 different kinds of out-of-plane angles φ and hence 20 core shift angles ψ are considered. So that there are in total CE 400 tilt boundaries for each elemental metal. Calculations were performed with LAMMPS software, using molecular statics and the embedded-atom-method (EAM) interatomic potentials and the third-generation charge-optimized-many--body (COMB3) potential [19,20, 28-31]. The boundary structures are visualized with OVITO [32].

3. Core shift results

The calculated grain boundary energy for copper and aluminum, with 17 different in-plane misorientation angles, as a function of core-shift angle are shown in Fig. 2(a) and 2(b), respectively. For clarity, results for three in-plane misorientation angles are not shown due to overlapping data [21]. Our calculated misorientation-dependent energy of boundaries with high-symmetry tilt axes along [001], [110] and [111] were carefully compared with published results and the consistency and accuracy of our calculations was confirmed [8,33,34]. For each in-plane misorientation angle, 20 core-shift angles are considered. Core-shift angles 0, 19.47°, 54.74° and −35.26° correspond to tilt axes or boundary core along [111], [112], [001] and [110], respectively.

Taking GB [111] 60° for example (on purple curves in Fig. 2) listed in Table 1, it is the incoherent twin boundary with the reciprocal of the density of coincident sites $\Sigma = 3$ and boundary normal $[1\bar{2}1]$ and $[2\bar{1}\bar{1}]$ for the black and white crystals, respectively [35,36]. From this boundary, the coherent twin boundary is obtained through core shifting, which has a composite tilt axis [110], a composite misorientation angle 70.53° and boundary normal $[1\bar{1}1]$ and $[1\bar{1}\bar{1}]$ for the black and white crystals, respectively [37]. In general, the composite misorientation angle is given by $\cos(\boldsymbol{\gamma}/2) = \cos(\boldsymbol{\theta}/2)\cdot\cos(\boldsymbol{\varphi}/2)$ following the geometry analysis with the Rodrigues vector [14,21], where $\boldsymbol{\gamma}$ is the composite rotation angle, $\boldsymbol{\theta}$ is the in-plane misorientation angle and $\boldsymbol{\varphi}$ is the out-of-plane angle [21,22]. From this boundary, Σ11 and single crystal can also be obtained. The composite tilt axis for the Σ11 boundary is [112], the composite misorientation angle is 62.96°, and the boundary normal are $[1\bar{3}1]$ and $[3\bar{1}\bar{1}]$ for the black and white crystal, respectively.

For the purpose of energy scaling, we only consider data involving the composite tilt axes or boundary core between [552] to [113], or core shift angles from −19.47° to 29.50° and mean boundary plane $(1\bar{1}0)$, in contrast to boundaries with [111] tilt axis and $(\bar{1}12)$ mean boundary plane [38,39]. We select this subset of the data because we have previously shown that within this range the grain boundary energy variation is linear with the jog density within the cores [21], which we show below facilitates analysis of the scaling behavior. Within this range, Table 2 shows that the maximum composite misorientation angles after core shift for GB [111] 13.17° with boundary cores between [552] and [113] are still ∼ 15°. Table 2 also shows that the core-shift boundary from GB [111] 13.17° with boundary core along [001] has a composite misorientation angle 22.62°, which is clearly out of the misorientation angle range for a low angle boundary.

3.1. Pairwise comparisons

We show the pairwise comparison of CE grain boundary energies for Al and Cu in Fig. 3(a). Clearly there is a poor scaling relationship with many data points off the fitted proportional line, which is consistent with previous publications [5,8]. The constant for these two groups of CE 200 grain boundaries is 1.71 close to the proportionality constant of 1.783 derived from the data set calculated with the same EAM potentials by Tschopp et al. [8]. In contrast, the pairwise comparison of the same group of CE boundaries for Cu and Ni, that for Cu and Pt, shown in Fig. 3 (b-c), and that for Cu and Au in Fig. S1, all show good proportionality relationship as reported previously [5]. In Fig. 3(d) we show the scaling of boundaries with [111] tilt axis or a core shift angle of zero. Clearly the scaling constant 1.63 for low angle boundaries (0 ∼ 15°) and that 1.74 for all [111] boundaries (0 ∼ 60°) are different.

3.2. Energy scaling for different in-plane misorientation angles

To elucidate the dependence of the scaling behavior on the boundary structure at the atomic scale, we first classify all the data by the in-plane misorientation angle and show data points associated with different in-plane misorientation angles in Fig. 3(a)–(c) using different shapes and colors. Different points with the same shape and color correspond to a set of boundaries, obtained from the same in-plane misorientation angle followed by different out-of-plane rotations (see Fig. 1c), with different composite rotation axes in the $(1\bar{1}0)$ plane and core-shift angles. We classify as subgroups boundaries with the same in-plane misorientation

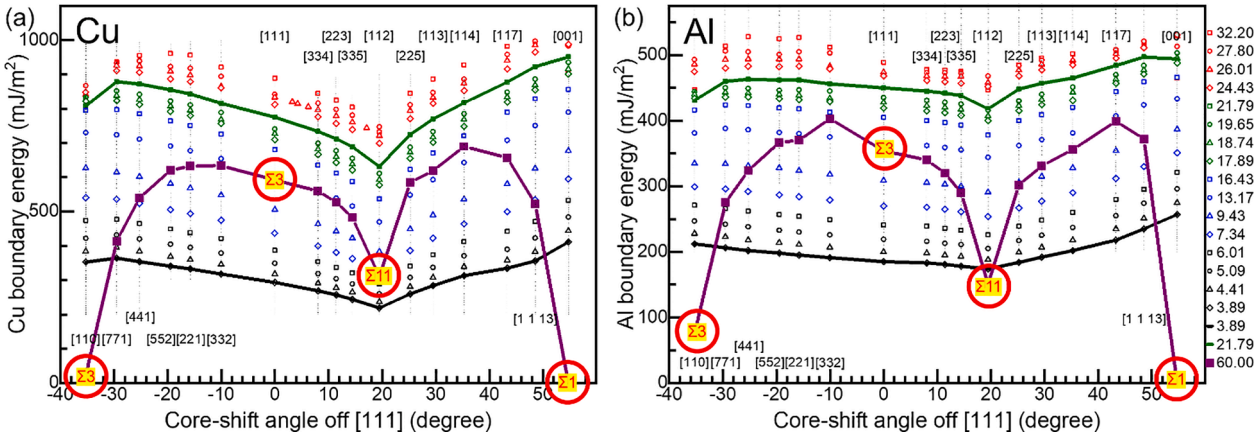

Fig. 2. Core-shift angle dependent boundary energy.
Grain boundary energy in copper and aluminum as a function of the core shift angle. Core-shift angles 0, 19.47°, 54.74° and −35.26° correspond to boundary core direction [111], [112], [001] and [110], respectively. GB [111] 60° is the incoherent twin boundary, from which the coherent twin boundary [37] (rotation axis [110], rotation angle 70.53°, mean boundary plane $(1\bar{1}0)$]) is obtained through core shifting. Different colors and shapes in the legend on the right are used to denote different in-plane misorientation angles. Three curves in each panel are drawn as a guide to eyes.

Table 1
Geometrical specification of GB [111] 60.00° with different core shift angles.
Starting from the composite rotation axes, we calculated the boundary normal, period vectors and the composite misorientation angles due to the core shift process. Both before and after the core shift, the mean boundary normal keeps $[1\bar{1}0]$. The composite angle is given by $\cos(\gamma/2) = \cos(\theta/2)\cdot\cos(\varphi/2)$. It can also be calculated from the Miller's indexes for two period vectors since it is the symmetrical tilt grain boundaries. The Miller indexes for the composite rotation axes are rewritten in Cartesian coordinate system with three unit vectors $e_1 = [\bar{1}\bar{1}2]/\sqrt{6}$, $e_2 = [1\bar{1}0]/\sqrt{2}$, and $e_3 = [111]/\sqrt{3}$.

Composite rotation axis l	$tan\psi$	Core-shift angle ψ(°)	$\tan(\varphi/2) = \tan\psi\cdot\sin\frac{\theta}{2}$	$cos\frac{\gamma}{2}$	Composite rotation angle γ(°)	Composite boundary normal $n2_b$ $n2_w$	Composite period vector $p2_b$ $p2_w$
[110] $e_3 - \sqrt{2}/2e_1$	$-\frac{\sqrt{2}}{2}$	− 35.26	$-\frac{1}{2\sqrt{2}}$	$\frac{\sqrt{2}}{\sqrt{3}}$	70.53	[1 $\bar{1}$ 1] [1 $\bar{1}$ $\bar{1}$]	[$\bar{1}$ 1 2] [1 $\bar{1}$ 2]
[111] e_3	0	0	0	$\frac{\sqrt{3}}{2}$	60	[1 $\bar{2}$ 1] [2 $\bar{1}$ $\bar{1}$]	[$\bar{1}$01] [0$\bar{1}$1]
[112] $e_3 + \sqrt{2}/4e_3$	$\frac{\sqrt{2}}{4}$	19.47	$\frac{\sqrt{2}}{8}$	$\frac{\sqrt{8}}{\sqrt{11}}$	62.96	[1$\bar{3}$1] [3$\bar{1}\bar{1}$]	[$\bar{7}$14] [$\bar{1}$74]
[001] $e_3 + \sqrt{2}/1e_1$	$\frac{\sqrt{2}}{1}$	54.74	$\frac{1}{\sqrt{2}}$	$\frac{1}{\sqrt{2}}$	90	[0 $\bar{1}$ 0] [1 0 0]	[$\bar{1}$00] [0$\bar{1}$0]

Table 2
Geometrical specification of GB [111] 13.17° with different core shift angles.
Before the core-shift, the rotation axis is [111], the rotation angle is $\tan(\theta/2) = 1/5\sqrt{3}$ and the mean boundary normal is $[1\bar{1}0]$. The Miller indexes for the composite rotation axes are rewritten in Cartesian coordinate system with three unit vectors $e_1 = [\bar{1}\bar{1}2]/\sqrt{6}$, $e_2 = [1\bar{1}0]/\sqrt{2}$, and $e_3 = [111]/\sqrt{3}$.

Composite rotation axis l	$tan\psi$	Core-shift angle ψ(°)	$\tan(\varphi/2) = \tan\psi\cdot\sin\frac{\theta}{2}$	$cos\frac{\gamma}{2}$	Composite rotation angle γ(°)	Composite boundary normal $n2_b$ $n2_w$	Composite period vector $p2_b$ $p2_w$
[110] $e_3 - \sqrt{2}/2e_1$	$-\frac{\sqrt{2}}{2}$	− 35.26	$\frac{-1}{\sqrt{152}}$	$\frac{\sqrt{50}}{\sqrt{51}}$	16.10	[5 $\bar{5}$ 1] [5 $\bar{5}$ $\bar{1}$]	[$\bar{1}$ 1 10] [1 $\bar{1}$ 10]
[552] $e_3 - \sqrt{2}/4e_1$	$-\frac{\sqrt{2}}{4}$	19.47	$\frac{-1}{\sqrt{608}}$	$\frac{\sqrt{200}}{\sqrt{203}}$	13.96	[29 $\bar{31}$ 5] [31 $\bar{29}$ $\bar{5}$]	[$\bar{29}$ $\bar{11}$ 100] [$\bar{11}$ $\bar{29}$ 100]
[111] $e_3 + 0\ e_1$	0	0	0	$\frac{\sqrt{75}}{\sqrt{76}}$	13.17	[7 $\bar{8}$ 1] [8 $\bar{7}$ $\bar{1}$]	[$\bar{3}\bar{2}$5] [$\bar{2}$35]
[112] $e_3 + \sqrt{2}/4e_1$	$\frac{\sqrt{2}}{4}$	19.47	$\frac{1}{\sqrt{608}}$	$\frac{\sqrt{200}}{\sqrt{203}}$	13.96	[9 $\bar{11}$ 1] [11 $\bar{9}$ $\bar{1}$]	[$\bar{23}$ $\bar{17}$ 20] [$\bar{17}$ $\bar{23}$ 20]
[113] $e_3 + 2\sqrt{2}/5e_1$	$\frac{2\sqrt{2}}{5}$	29.50	$\frac{\sqrt{2}}{5\sqrt{19}}$	$\frac{25\sqrt{3}}{2\sqrt{477}}$	15.11	[11 $\bar{14}$ 1] [14 $\bar{11}$ $\bar{1}$]	[$\bar{43}$ $\bar{32}$ 25] [$\bar{32}$ $\bar{43}$ 25]
[001] $e_3 + \sqrt{2}/1e_1$	$\frac{\sqrt{2}}{1}$	54.74	$\frac{1}{\sqrt{38}}$	$\frac{\sqrt{25}}{\sqrt{26}}$	22.62	[2 $\bar{3}$ 0] [3 $\bar{2}$ 0]	[$\bar{3}$ $\bar{2}$ 0] [$\bar{2}$ $\bar{3}$ 0]

angle but different core-shift angles. A review of Fig. 3(a) shows that for the pairwise comparison of copper and aluminum each boundary subgroup shows different slopes with different finite non-zero intercepts. In contrast, Fig. 3(b) and (c) shows the pairwise comparison of copper and nickel and copper and platinum, which do not exhibit this type of behavior. Moreover, in Fig. 3(a) there is a systematic scatter for low angle boundaries with in-plane misorientation angle less than 15° and for high angle boundaries with in-plane misorientation angle between 15° and 32.20° On the other hand, for high angle GBs with in-plane misorientation angles above 32.20°, the variation in the proportional scaling is considerably reduced. Fig. 3(d) shows data points that exclude core shift in the $(1\bar{1}0)$ plane, so that all boundaries have [111] tilt axes, and from which the proportionality constant for all and low angle boundaries are 1.74 and 1.63, respectively. This means that when exclusively low and even high angle [111] boundaries with in-plane misorientation angle between 15° and 32.20° are considered, there is still a dependence of the scaling constant on the in-plane misorientation angle. A similar fit to the high angle boundary data yields a scaling constant of 1.80, as shown in Fig. 3(e). Remarkably, this scaling constant value (1.80) sets the upper limit for the combined low angle and high angle (with in-plane misorientation angle between 15° and 32.20°) GB data sets, as shown in Fig. 3(f).

We now focus on the CE boundary energies for subgroups with in-plane misorientation angles of 3.89° and 16.43°. These boundaries are representative of the behavior of low angle boundaries and their scaling behavior are detailed in Fig. 4(a) and (b), respectively. For each in-plane misorientation angle, we consider 10 different core-shift angles within the $(1\bar{1}0)$ plane. Clearly the boundary energies vary according to the composite rotation axes and in both cases the energy reaches its minimum when the tilt axis lies along [112], which lies in the close packed $(11\bar{1})$ plane [21]. Since low angle boundaries are known to dissociate, this behavior reflects the effect of dislocation dissociation on boundary energies as the composite rotation axis shifts into and out of the close packed plane.

Fig. 4(c) shows the slope and intercepts for all subgroups with low and high angles with in-plane misorientation angle between 15° and 32.20°. Each subgroup exhibits a different slope and intercept, consistent with the earlier analysis by Tschopp et al. [8]. Low angle boundaries can be viewed as an array of dislocations, whose dissociation is sensitive to the core-shift angle within the $(1\bar{1}0)$ plane. On the other hand, high angle boundaries do not dissociate and hence show no dependence on core-shift angle. In this scissor-shaped diagram there is a strong initial positive (negative) dependence of the slope (intercept) with increasing in-plane misorientation angle, followed by an abrupt switch in this trend

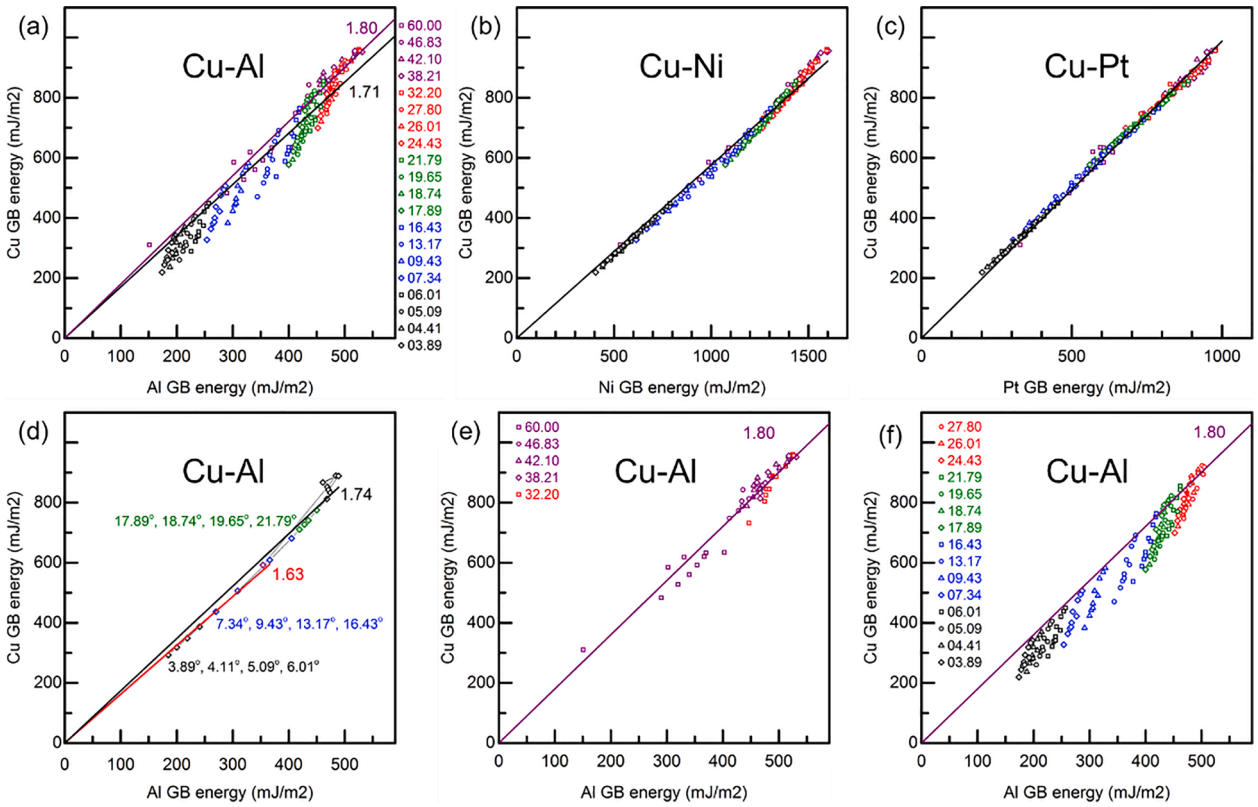

Fig. 3. Comparison of grain boundary energies in Cu and Al.
(a) Comparison of grain boundary energies calculated for copper and aluminum and proportional fit of all the data points. Data points are coloured by the in-plane misorientation angles. 20 different in-plane misorientation angles are listed in the legend. Multiple data point of the same colour and shape reflect the different core-shift angles. The slope of 1.71 is a best fit to all CE 200 boundaries. The 1.80 slope is the scaling for high angle boundaries. (b-c) Comparison of grain boundary energies calculated for nickel and platinum. (d) Comparison of grain boundary energies with composite rotation axis along [111] only (grain boundaries without out-of-plane rotation, as shown in Fig. 1b). The in-plane misorientation angles are shown next to corresponding grouping of data points. Proportional fit of low angle boundaries (black and blue data points) shown as a red line (slope 1.63). (e) Proportional fit of high angle boundaries energies with in-plane misorientation angles above 32.20. (f) Comparison of grain boundaries energies with in-plane misorientation angle less than 32.20°.

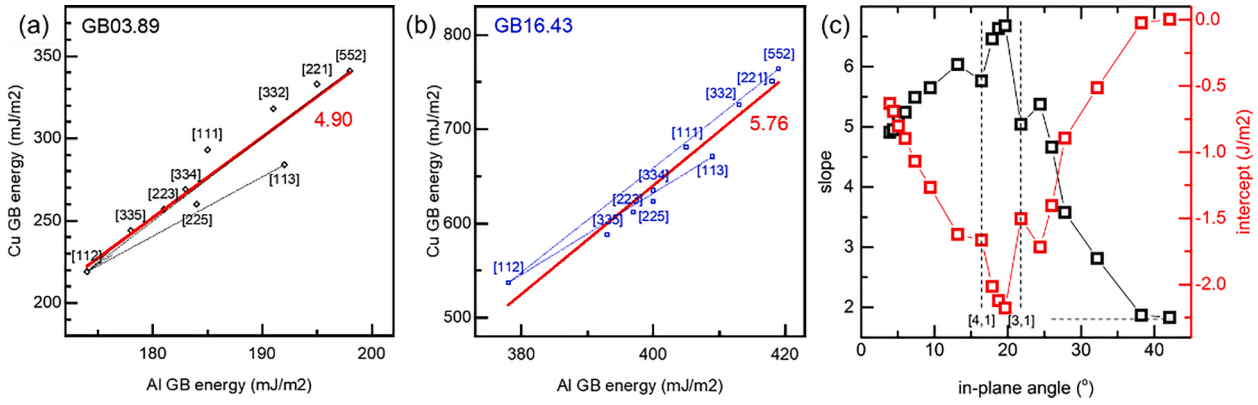

Fig. 4. Dependence of the linear fitting on in-plane misorientation angle.
(a) Comparison of grain boundary energies with in-plane misorientation angle 3.89° and different core-shift angles together with a linear fit (slope 4.09). (b) Comparison of grain boundary energies with in-plane misorientation angle 16.43° and different core-shift angles together with a linear fit (slope 5.76). (c) the dependence of the slope and intercept on in-plane misorientation angles from the linear fitting of all in-plane misorientation angles up to 42.10°.

at $\theta = 19.65°$ and subsequently followed by an angle-independent behavior beyond $\theta = 38.21°$. In addition, we note the slope and intercept plots exhibit cusps at delimiting boundaries [4,1] and [3,1] in the structural unit model, reflecting the importance of atomic structures within the boundary cores [40,41]. The slope of 1.80 and zero intercept found for the subgroup with even greater in-plane misorientation angles than 38.21° shown in Fig. 4(c) are consistent with the fixed scaling constant for high angle boundaries found in Fig. 3(e) regardless of core shift angle.

3.3. Core-shift angle dependent proportionality constant

Since the core-shift angle and the composite rotation axes are related to the jog density along boundary cores [21] and hence the degree to

which dislocations can dissociate, we reclassify the data again into small groups according to their core-shift angle. Fig. 5(a) shows data points for all 20 in-plane misorientation angles and 4 representative core-shift angles, − 19.47°, 0°, 19.47° and 29.50° that span the vast range of core-shift angles considered in this work. The corresponding composite rotation axes in $(1\bar{1}0)$ plane are [552], [111], [112] and [113], respectively. Axis [552] is the far shift away from [111] toward [110] that we have considered. Axis [112] is in the close-packed plane $(11\bar{1})$. Axis [113] is the far shift away from [111] toward [001]. For clarity, data points associated with the core-shift angles in-between are not shown. While Fig. 5(a) shows evidence of scatter, the scaling behavior of GBs with the same core-shift angle is markedly better. To this end, Fig. 5 (b) shows the data for the 7 low angles boundaries that comprised Fig. 5 (a) and from which the excellent scaling with core-shift angle is now evident. The proportionality constants for core-shift angles − 19.47°, 0°, 19.47° and 29.50° are 1.77, 1.63, 1.31 and 1.54, respectively. The lowest energy boundaries are associated with a [112] composite rotation axis with a core-shift angle of 19.47° and these same boundaries exhibit the lowest possible scaling constant 1.31. Fig. 5(c) shows the scaling constants for the low angle boundaries for each of the 10 core-shift angles considered in this study, with four data points taken from Fig. 5(b) highlighted. The dashed line corresponds to the scaling constant 1.80 (see Fig. 3e) observed for high angle boundaries that is approached by low angle boundaries at increasingly negative core-shift angles. There is a monotonic variation of the scaling constant on either side of the 19.47° core-shift angle, which is associated with a [112] composite rotation axis lying in the close-packed plane $(11\bar{1})$. In the two sides of [112] in the $(1\bar{1}0)$ plane, the decomposition of the tilt axes is different [21]. On the side of [110], the tilt axes are decomposed into [112] segments and [110] segments. On the other side, the tilt axes are decomposed into [112] segments and [001] segments. Hence there is a change in the trend of the scaling constant.

To gain a better understanding of the dependence of the proportional scaling constant on the core-shift angle, we examined the atomic structure variation of CE boundaries in copper and aluminum with an in-plane misorientation angle of 3.89° at each of the 10 core-shift angles (Fig. 6). The atoms are selected by the centrosymmetry parameters and colored according to atomic energy [42]. The grain boundaries are projected along their period vectors. Clearly, the copper dislocations are fully dissociated at the [112] composite rotation axis with two partials and stacking faults in-between. Atoms at the two partials have higher energy than those that comprise the stacking faults. In contrast, the aluminum dislocation at a [112] composite rotation axis is not dissociated, with the full dislocation core having the highest energy atoms at its center. This demonstrates that even without the confinement introduced by jogs that emerge at non-[112] composite rotation axes, stacking faults in aluminum are not dissociated [43]. In summary, the atoms in the copper boundary core are correlatively relaxed through the formation of extended stacking faults while the atoms in the aluminum boundary core are only locally relaxed. Even through the partial dislocation core in aluminum still can be identified, the two strongly-coupled partials are so close that the strain field and even the bonding distortion of two partials overlap, as shown in Fig. 6(b). The fact that the composite rotation axis lies in the close packed plane allows the formation of extended relaxed stacking fault structures in copper compared to the locally relaxed boundary core in aluminum and is responsible for the lowest possible proportional scaling constant. Alternatively, with regards to the Al boundary, the dislocation dissociation in the copper boundary, as an additional way to reduce boundary energy, decreases the proportional scaling constant.

When the composite rotation axis shifts away from [112] toward [552], the jog density in the copper boundary increases. The introduction of each jog shifts the boundary core from one close-packed $(11\bar{1})$ plane to a neighbouring $(11\bar{1})$ plane. This breaks up the extended relaxation along the core, while the distance between the two partials decreases and narrows the width of the stacking fault ribbon. Gradually the dislocation become undissociated. In these cases, boundary-core atoms in both copper and aluminum are locally relaxed and thus the proportional scaling constant approaches the 1.802 value associated with high angle boundaries, where the stacking fault effects are diminished (or eliminated). A similar analysis also applies when the composite rotation axis shifts towards [113].

For the case of boundaries with in-plane misorientation angles from 15° to 32.30°, as shown in Fig. 6(a), the dislocations are physically closer together so that their interaction increases in strength and the width of the splitting between partial becomes narrow so that a localized boundary core appears. Therefore, the relaxation mechanism of individual boundary atoms in copper and aluminum gradually become very similar, as shown in Fig. 3(e), so that the individual atomic relaxation is no longer important and only the crystallography plays a role, which yield a perfect proportional scaling. In this instance, the dependence of proportionality constants on the core-shift angle gradually disappears and the overall scaling approaches that of high angle boundaries.

4. Discussion

In this work we have explored the possible origin of the anomalous scaling of Al grain boundary energies. The unusual behavior of

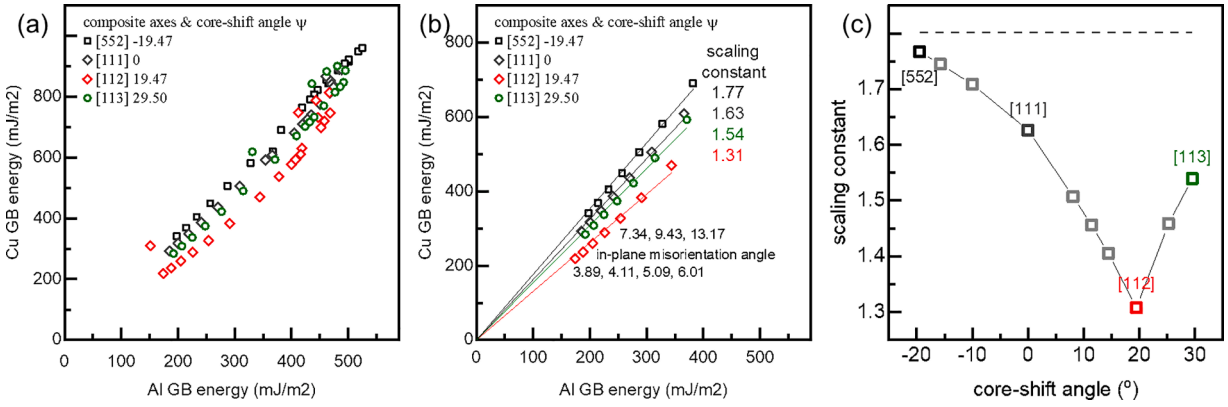

Fig. 5. Core shift dependent proportionality constant.
(a) Comparison of grain boundary energies for all in-plane misorientation angles with specified composite rotation axes or the core-shift angles referenced to [111]. (b) Proportional fitting of data points associated with seven low angle grain boundaries with composite rotation axis [552], [111], [112] and [113]. (c) Core-shift angle dependent proportional scaling constants as a function of core shift angle with the upper limit 1.80 (associated with large angle boundaries) shown as a dash line.

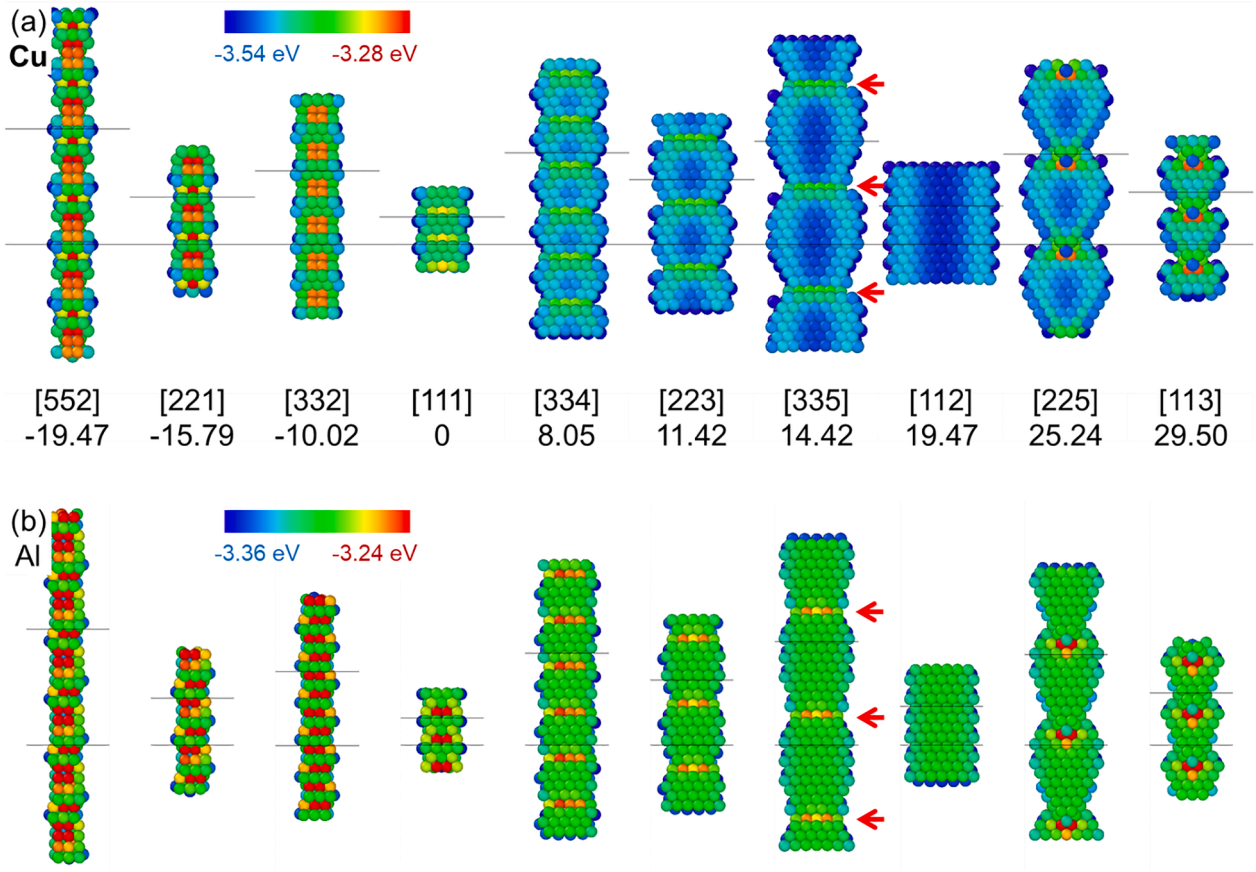

Fig. 6. Structural difference of GB3.89 in Cu and Al.
(a) Variation of grain boundary structures in copper, projected along the boundary period vector, with different core-shift angles and the corresponding composite rotation axis. (b) Variation of grain boundary structures in aluminium. Non-fcc copper atoms are selected by centrosymmetry parameters greater than 0.39 and aluminium atoms greater than 0.49 [42]. All atoms are coloured by energy. The length of each stacking fault ribbon is 3 times of the length of the corresponding vector below graph (a). The jog sites along the tilt axis [335] for copper and aluminium are highlighted by red arrows.

aluminum is usually attributed to its high stacking fault energy and low elastic anisotropy [5]. However, nickel also has a high stacking fault energy, as shown in Table 3, and still exhibits well defined proportional scaling relationships with respect to other fcc metal as shown in Fig. 3(b) and in the literature [5,43]. Hence the value of stacking fault energy cannot be the sole criterion. Considering the anisotropy of the Young's modulus, the shear modulus, and Poisson ratio, the quantification of the elastic anisotropy in terms of a single parameter is over simplified and unable to describe many physical properties [44], such as the differences in the proportionality constants for different boundaries in one element.

Table 3
Calculated material properties from each potential for f. c. c. metal.

	Au Foiles [31]	Cu Mishin [29]	Ni Mishin [30]	Al Mishin [30]	Pt Foiles [31]	Pt COMB3 [20]
Cohesive energy (eV)	−3.93	−3.54	−4.45	−3.36	−5.77	−5.77
Lattice constant (A)	4.08	3.615	3.52	4.05	3.92	3.92
Bulk modulus (GPa)	166.9	138.4	181.2	80.0	283.1	228
C11(GPa)	183.2	169.9	247.9	113.8	303.1	283
C12(GPa)	158.8	122.6	147.8	61.6	273.1	198
C44(GPa)	44.7	76.2	124.8	31.6	68.3	82
SF energy Γ	4.7	44.4	125.2	145.5	14.61	321
C44/Γ	9.5	1.7	1.0	0.22	4.7	0.26
Zener anisotropy index	3.7	3.2	2.5	1.2	4.6	1.9

Since the core-shift angle dependent scaling highlights the importance of the dissociation of dislocations, we explore the possibility that the dissociation width plays a role in scaling. The stacking fault width in isotropic materials is proportional to the ratio of the shear modulus to the stacking fault energy. Assuming the shear modulus can be described by C_{44}, closely related to the shear modulus in the dislocation model for the grain boundaries [45], we compared the ratio C_{44}/Γ for different elements and potentials and found that this ratio is possibly the most relevant for determining the scatter observed in the proportional scaling constant data [5,45]. For example, the ratio for Al and Pt-COMB3 are 0.22 and 0.26 (see Table 3), respectively. This suggests that the COMB3 potential for Pt, which is known to accurately describe the stacking fault energy and hence dissociation width in this metal, should show a similar behavior to that found in Al [20]. In contrast, the ratio for Cu, Ni and, in particular, Pt EAM potentials are 1.7, 1.0 and 4.7, respectively. Hence for these materials, there are wider stacking faults in bulk and correspondingly less scatter in the pairwise scaling.

To demonstrate that a similar C_{44}/Γ ratio compared to Al yields similar scaling, we undertook a pairwise comparison of the CE boundary energies in copper using the EAM potential and platinum using the COMB3 potential. The full comparison is shown in Fig. 7. As was the case with Al, Fig. 7(a) shows that high angle grain boundaries exhibit better proportional scaling than low angle and high angle boundaries with in-plane misorientation angle between 15° and 32.20°. In addition, Fig. 7(c) shows that the low angle boundaries in platinum also exhibit core-shift

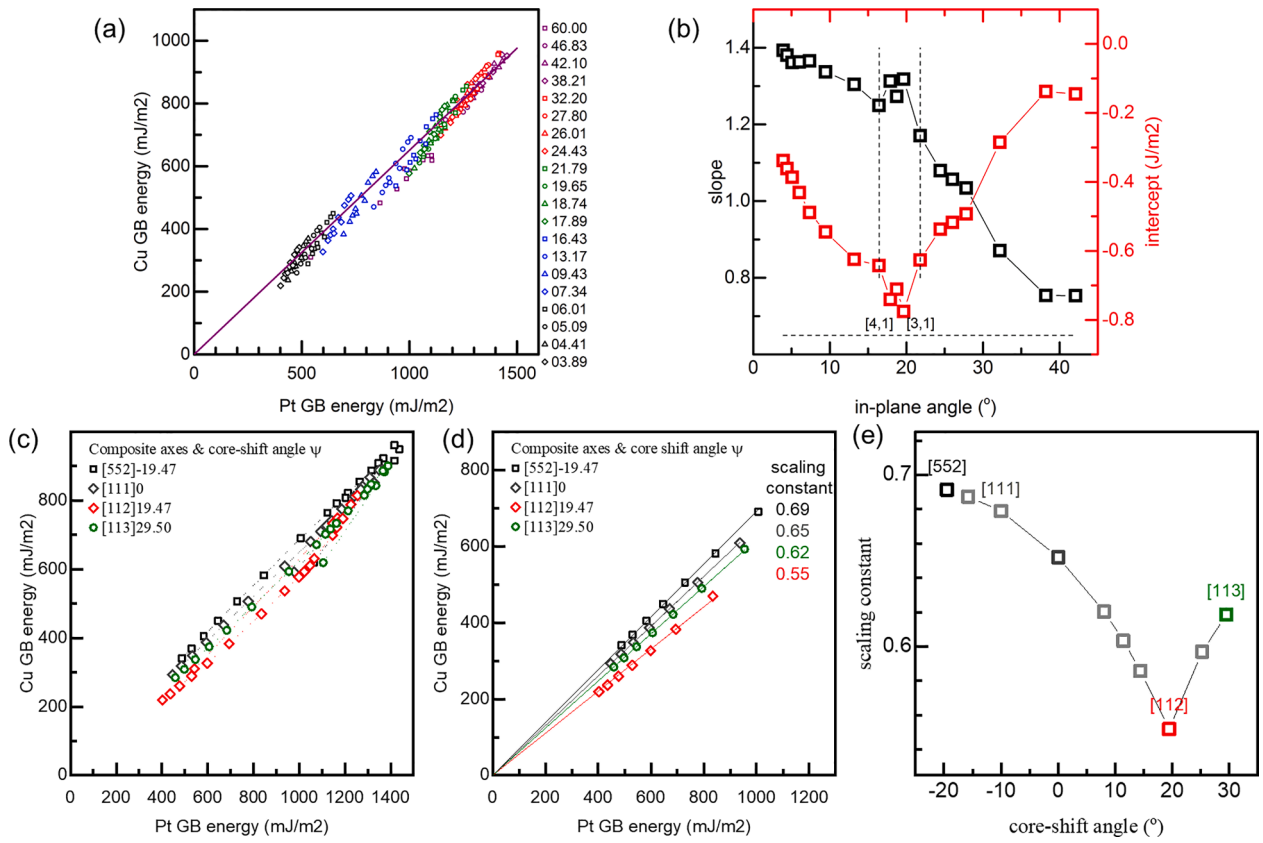

Fig. 7. Comparison of grain boundary energies in Cu and Pt.
(a) Comparison of grain boundary energies from EAM potential for copper and COMB3 potential for platinum. (b) in-plane misorientation angle dependent slope and intercept in linear fitting for in-plane misorientation angles up to 42.10°. (c) Comparison of grain boundary energies with specified composite rotation axes or the core-shift angles referenced to [111]. (d) Proportionality constants for four specified core-shift angles. (e) Core-shift angle dependent proportional scaling constants.

angle dependent proportional scaling constants, the detailed analysis of which is shown for four different core-shift angles in Fig. 7(d). The core-shift angle dependent scaling constant in Fig. 7(e) exhibits the same kind of variation as was found for Al in Fig. 5(c). Clearly the detailed pairwise scaling of Cu and Pt using the COMB3 potential is strikingly similar to that found in Al, hence confirming the ratio C_{44}/Γ is a good predictor of the expected scaling behaviour.

Apart from local relaxation and dislocation dissociation, there are many other kinds of boundary relaxation phenomena such as structural unit formation, faceting, 9R-phase or stacking fault related boundary dissociation, and interface phase (complexion) transitions [38,46–48]. We believe that all these different types of relaxation should be reflected in the pairwise comparison [1,49]. Our calculation shows that [100] boundaries in copper and aluminum show good scaling behavior but [110] boundaries show complex behavior and poor scaling in the pairwise comparison, which is likely related to the stacking fault related boundary dissociation in copper [50–52], instead of simple structural units [40,53,54].

5. Conclusion

The scatter in the pairwise comparison of Cu and Al exhibits both an in-plane misorientation angle and core-shift angle dependence, which indicates that in addition to crystallography, different varieties of individual atom relaxation make an important contribution to grain boundary energy and hence the scaling constants. The dislocation dissociation mechanism that correlates individual atomic relaxation in copper does not exist in aluminum, which is responsible for the large scatter in the pairwise comparison of CE boundaries, in particular low angle boundaries, where relaxation via dislocation dissociation in copper is dominant.

J.J.B and X.Z. acknowledge support from Science Foundation Ireland grants (12/RC/2278_P2 and 16/IA/4462), thank Adrian Sutton for helpful discussions and Trinity Centre for High Performance Computing for providing the computing resource.

Declaration of Competing Interest

The authors declare that they have no known competing financial interests or personal relationships that could have appeared to influence the work reported in this paper.

Supplementary materials

Supplementary material associated with this article can be found, in the online version, at doi:10.1016/j.actamat.2023.119606.

References

[1] A.P. Sutton, R.W. Balluffi, Interfaces in Crystalline Materials, OUP Oxford, 2006.
[2] J. Han, V. Vitek, D.J. Srolovitz, Grain-boundary metastability and its statistical properties, Acta Mater. 104 (2016) 259–273.
[3] D. Udler, D.N. Seidman, Grain boundary and surface energies of fcc metals, Phys. Rev. B Condens. Matter 54 (16) (1996) R11133–R11136.
[4] D.L. Olmsted, S.M. Foiles, E.A. Holm, Survey of computed grain boundary properties in face-centered cubic metals: I. Grain boundary energy, Acta Mater. 57 (13) (2009) 3694–3703.
[5] E.A. Holm, D.L. Olmsted, S.M. Foiles, Comparing grain boundary energies in face-centered cubic metals: Al, Au, Cu and Ni, Scr. Mater. 63 (9) (2010) 905–908.
[6] S. Ratanaphan, D.L. Olmsted, V.V. Bulatov, E.A. Holm, A.D. Rollett, G.S. Rohrer, Grain boundary energies in body-centered cubic metals, Acta Mater. 88 (2015) 346–354.
[7] V.V. Bulatov, B.W. Reed, M. Kumar, Grain boundary energy function for fcc metals, Acta Mater. 65 (2014) 161–175.

[8] M.A. Tschopp, S.P. Coleman, D.L. McDowell, Symmetric and asymmetric tilt grain boundary structure and energy in Cu and Al (and transferability to other fcc metals), Integr. Mater. Manuf. Innov. 4 (1) (2015) 1–14.
[9] A. Ayadi, H. Laib, O. Khalfallah, Relationship between structure and energy of symmetric tilt grain boundaries in Ag and Ni, Acta Phys. Pol. A 138 (3) (2020) 528–532.
[10] A.P. Sutton, Electronic Structure of Materials, Clarendon Press, 1993.
[11] J.H. Rose, J.R. Smith, F. Guinea, J. Ferrante, Universal features of the equation of state of metals, Phys. Rev. B 29 (6) (1984) 2963–2969.
[12] G.S. Rohrer, Grain boundary energy anisotropy: a review, J. Mater. Sci. 46 (18) (2011) 5881–5895.
[13] N.J. Schrenker, Z. Xie, P. Schweizer, M. Moninger, F. Werner, N. Karpstein, M. Mačković, G.D. Spyropoulos, M. Göbelt, S. Christiansen, C.J. Brabec, E. Bitzek, E. Spiecker, Microscopic deformation modes and impact of network anisotropy on the mechanical and electrical performance of five-fold twinned silver nanowire electrodes, ACS Nano 15 (1) (2021) 362–376.
[14] X. Zhang, J. Han, J.J. Plombon, A.P. Sutton, D.J. Srolovitz, J.J. Boland, Nanocrystalline copper films are never flat, Science 357 (6349) (2017) 397–400.
[15] J. Han, S.L. Thomas, D.J. Srolovitz, Grain-boundary kinetics: a unified approach, Prog. Mater. Sci. 98 (2018) 386–476.
[16] A. Bhattacharya, Y.F. Shen, C.M. Hefferan, S.F. Li, J. Lind, R.M. Suter, C.E. Krill, G. S. Rohrer, Grain boundary velocity and curvature are not correlated in Ni polycrystals, Science 374 (6564) (2021) 189–193.
[17] C. Woodward, D.R. Trinkle, L.G. Hector, D.L. Olmsted, Prediction of dislocation cores in aluminum from density functional theory, Phys. Rev. Lett. 100 (4) (2008).
[18] G. Lu, N. Kioussis, V.V. Bulatov, E. Kaxiras, Generalized-stacking-fault energy surface and dislocation properties of aluminum, Phys. Rev. B 62 (5) (2000) 3099–3108.
[19] T. Liang, T.R. Shan, Y.T. Cheng, B.D. Devine, M. Noordhoek, Y.Z. Li, Z.Z. Lu, S. R. Phillpot, S.B. Sinnott, Classical atomistic simulations of surfaces and heterogeneous interfaces with the charge-optimized many body (COMB) potentials, Mater. Sci. Eng. R 74 (9) (2013) 255–279.
[20] A.C. Antony, S.A. Akhade, Z. Lu, T. Liang, M.J. Janik, S.R. Phillpot, S.B. Sinnott, Charge optimized many body (COMB) potentials for Pt and Au, J. Phys. Condens. Matter 29 (22) (2017).
[21] X. Zhang, J.J. Boland, Universal preference for low-energy core-shifted grain boundaries at the surfaces of fcc metals, Phys. Rev. Res. 5 (1) (2023), 013223.
[22] X. Zhang, M. Wang, H. Wang, M. Upmanyu, J.J. Boland, Restructuring of emergent grain boundaries at free surfaces – An interplay between core stabilization and elastic stress generation, Acta Mater. 242 (2023), 118432.
[23] X. Zhang, I. Demirel, J.J. Boland, Wedge disclination description of emergent core-shifted grain boundaries at free surfaces, Scr. Mater. 234 (2023), 115562.
[24] J. Schiotz, K.W. Jacobsen, Nanocrystalline metals: roughness in flatland, Nat. Mater. 16 (11) (2017) 1059–1060.
[25] M.A. Tschopp, D.L. McDowell, Structures and energies of Sigma 3 asymmetric tilt grain boundaries in copper and aluminium, Philos. Mag. 87 (22) (2007) 3147–3173.
[26] M.A. Tschopp, D.L. McDowell, Asymmetric tilt grain boundary structure and energy in copper and aluminium, Philos. Mag. 87 (25) (2007) 3871–3892.
[27] A.P. Sutton, E.P. Banks, A.R. Warwick, The five-dimensional parameter space of grain boundaries, Proc. R. Soc. A Math. Phys. 471 (2181) (2015).
[28] S. Plimpton, Fast parallel algorithms for short-range molecular-dynamics, J. Comput. Phys. 117 (1) (1995) 1–19.
[29] Y. Mishin, M.J. Mehl, D.A. Papaconstantopoulos, A.F. Voter, J.D. Kress, Structural stability and lattice defects in copper: ab initio, tight-binding, and embedded-atom calculations, Phys. Rev. B 63 (22) (2001), 224106.
[30] Y. Mishin, D. Farkas, M.J. Mehl, D.A. Papaconstantopoulos, Interatomic potentials for monoatomic metals from experimental data and *ab initio* calculations, Phys. Rev. B 59 (5) (1999) 3393–3407.
[31] S.M. Foiles, M.I. Baskes, M.S. Daw, Embedded-atom-method functions for the fcc metals Cu, Ag, Au, Ni, Pd, Pt, and their alloys, Phys. Rev. B Condens. Matter 33 (12) (1986) 7983–7991.
[32] A. Stukowski, Visualization and analysis of atomistic simulation data with OVITO-the open visualization tool, Model. Simul. Mater. Sci. 18 (1) (2010), 015012.
[33] A.D. Banadaki, M.A. Tschopp, S. Patala, An efficient Monte Carlo algorithm for determining the minimum energy structures of metallic grain boundaries, Comput. Mater. Sci. 155 (2018) 466–475.
[34] K. Wang, W.G. Zhang, J.Q. Xu, W.J. Dan, The impact of misorientation on the grain boundary energy in bi-crystal copper: an atomistic simulation study, J. Mol. Model. 28 (2) (2022).
[35] L. Liu, J. Wang, S.K. Gong, S.X. Mao, High resolution transmission electron microscope observation of zero-strain deformation twinning mechanisms in Ag, Phys. Rev. Lett. 106 (17) (2011), 175504.
[36] K. Lu, L. Lu, S. Suresh, Strengthening materials by engineering coherent internal boundaries at the nanoscale, Science 324 (5925) (2009) 349–352.
[37] F. Sansoz, J.F. Molinari, Mechanical behavior of Σ tilt grain boundaries in nanoscale Cu and Al: a quasicontinuum study, Acta Mater. 53 (7) (2005) 1931–1944.
[38] T. Meiners, T. Frolov, R.E. Rudd, G. Dehm, C.H. Liebscher, Observations of grain-boundary phase transformations in an elemental metal, Nature 579 (7799) (2020) 375–378.
[39] L. Frommeyer, T. Brink, R. Freitas, T. Frolov, G. Dehm, C.H. Liebscher, Dual phase patterning during a congruent grain boundary phase transition in elemental copper, Nat. Commun. 13 (1) (2022) 3331.
[40] A.P. Sutton, V. Vitek, On the structure of tilt grain boundaries in cubic metals I. Symmetrical tilt boundaries, Philos. Trans. R. Soc. Lond. Math. Phys. Sci. 309 (1506) (1983) 1–36.
[41] J. Han, V. Vitek, D.J. Srolovitz, The grain-boundary structural unit model redux, Acta Mater. 133 (2017) 186–199.
[42] C.L. Kelchner, S.J. Plimpton, J.C. Hamilton, Dislocation nucleation and defect structure during surface indentation, Phys. Rev. B 58 (17) (1998) 11085–11088.
[43] J.P. Hirth, J. Lothe, Theory of Dislocations, McGraw-Hill, 1982.
[44] A. Marmier, Z.A.D. Lethbridge, R.I. Walton, C.W. Smith, S.C. Parker, K.E. Evans, ElAM: a computer program for the analysis and representation of anisotropic elastic properties, Comput. Phys. Commun. 181 (12) (2010) 2102–2115.
[45] W.T. Read, W. Shockley, Dislocation models of crystal grain boundaries, Phys. Rev. 78 (3) (1950) 275–289.
[46] P.R. Cantwell, T. Frolov, T.J. Rupert, A.R. Krause, C.J. Marvel, G.S. Rohrer, J. M. Rickman, M.P. Harmer, Grain boundary complexion transitions, Annu. Rev. Mater. Res. 50 (1) (2020) 465–492.
[47] P.R. Cantwell, M. Tang, S.J. Dillon, J. Luo, G.S. Rohrer, M.P. Harmer, Grain boundary complexions, Acta Mater. 62 (2014) 1–48.
[48] M.P. Harmer, G.S. Rohrer, Grain boundary complexions - current status and future directions, Curr. Opin. Solid State Mater. Sci. 20 (5) (2016). Iv-V.
[49] A.P. Sutton, R.W. Balluffi, Overview .61. On geometric criteria for low interfacial energy, Acta Metall. 35 (9) (1987) 2177–2201.
[50] J.D. Rittner, D.N. Seidman, <110>symmetric tilt grain-boundary structures in fcc metals with low stacking-fault energies, Phys. Rev. B Condens. Matter 54 (10) (1996) 6999–7015.
[51] J.D. Rittner, D.N. Seidman, K.L. Merkle, Grain-boundary dissociation by the emission of stacking faults, Phys. Rev. B 53 (8) (1996) R4241–R4244.
[52] D.E. Spearot, K.I. Jacob, D.L. McDowell, Dislocation nucleation from bicrystal interfaces with dissociated structure, Int. J. Plasticity 23 (1) (2007) 143–160.
[53] A.P. Sutton, V. Vitek, On the structure of tilt grain boundaries in cubic metals II. Asymmetrical tilt boundaries, Philos. Trans. R. Soc. Lond. Math. Phys. Eng. Sci. 309 (1506) (1983) 37–54.
[54] A.P. Sutton, V. Vitek, On the structure of tilt grain boundaries in cubic metals. III. Generalizations of the structural study and implications for the properties of grain boundaries, Philos. Trans. R. Soc. Lond. Math. Phys. Sci. 309 (1506) (1983) 55–68.